nature portfolio

https://doi.org/10.1038/s41586-026-10703-4

Supplementary information

Chromatin landscape and epigenetic heterogeneity of acute myeloid leukaemia

In the format provided by the authors and unedited

Supplementary Information

Chromatin landscape and epigenetic heterogeneity of acute myeloid leukemia

Yotaro Ochi✉, Markus Liew-Littorin, Yasuhito Nannya, Sofia Bengtzen, Benedicte Piauger, Stefan Deneberg, Martin Jädersten, Vladimir Lazarevic, Jörg Cammenga, Anna Robelius, Lovisa Wennström, Emma Ölander, Senji Kasahara, Nobuhiro Hiramoto, Nobuhiro Kanemura, Nobuo Sezaki, Maki Sakurada, Makoto Iwasaki, Junya Kanda, Yasunori Ueda, Satoshi Yoshihara, Tom Erkers, Nona Struyf, Yu Watanabe, Masanori Motomura, Masahiro M Nakagawa, Ryunosuke Saiki, Hidehito Fukushima, Koji Okazaki, Suguru Morimoto, Akinori Yoda, Rurika Okuda, Shintaro Komatsu, Guoxiang Xie, Albin Österroos, Ayana Kon, Lanying Zhao, Yuichi Shiraishi, Takayuki Ishikawa, Satoru Miyano, Kotoe Katayama, Seiya Imoto, Shuichi Matsuda, Akifumi Takaori-Kondo, Hiroyuki Aburatani, Hiroshi I Suzuki, Olli Kallioniemi, Gunnar Juliusson, Martin Höglund, Sören Lehmann✉, Seishi Ogawa✉

Table of Contents

Supplementary Table 10. Gene sets used for GSEA and GO analysis

Supplementary Table 11. Genes used for RNA-based prediction models (ClaNC)

Supplementary Fig. 1

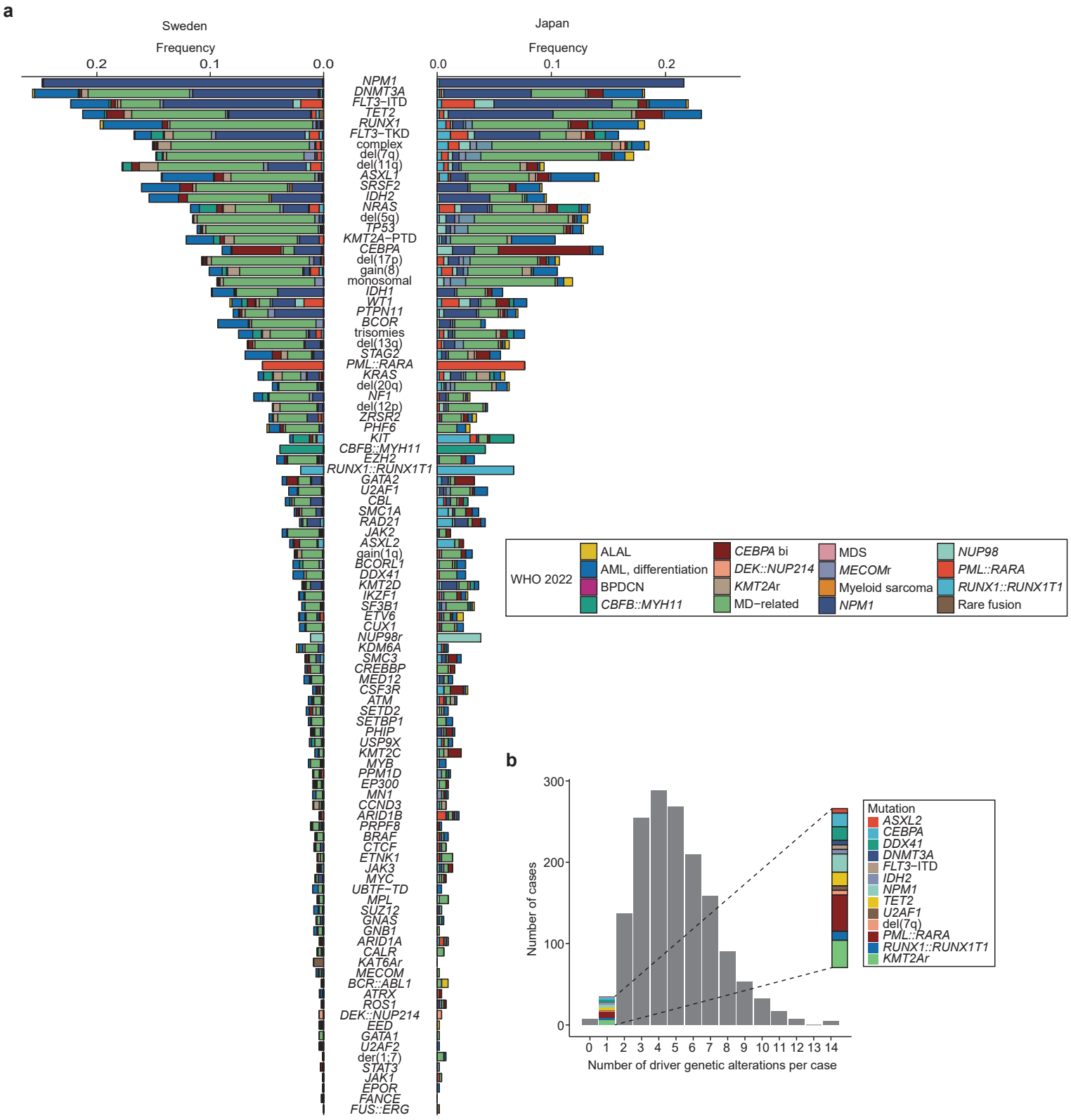

Supplementary Fig. 1 | Summary of driver genetic alterations. a. Frequencies of genetic alterations in Swedish and Japanese cohorts. Each color represents WHO 2022 diagnosis. **b.** Number of driver genetic alterations per sample is shown as a barplot. In samples with only one alteration, the specific alteration is highlighted.

Supplementary Fig. 2

a

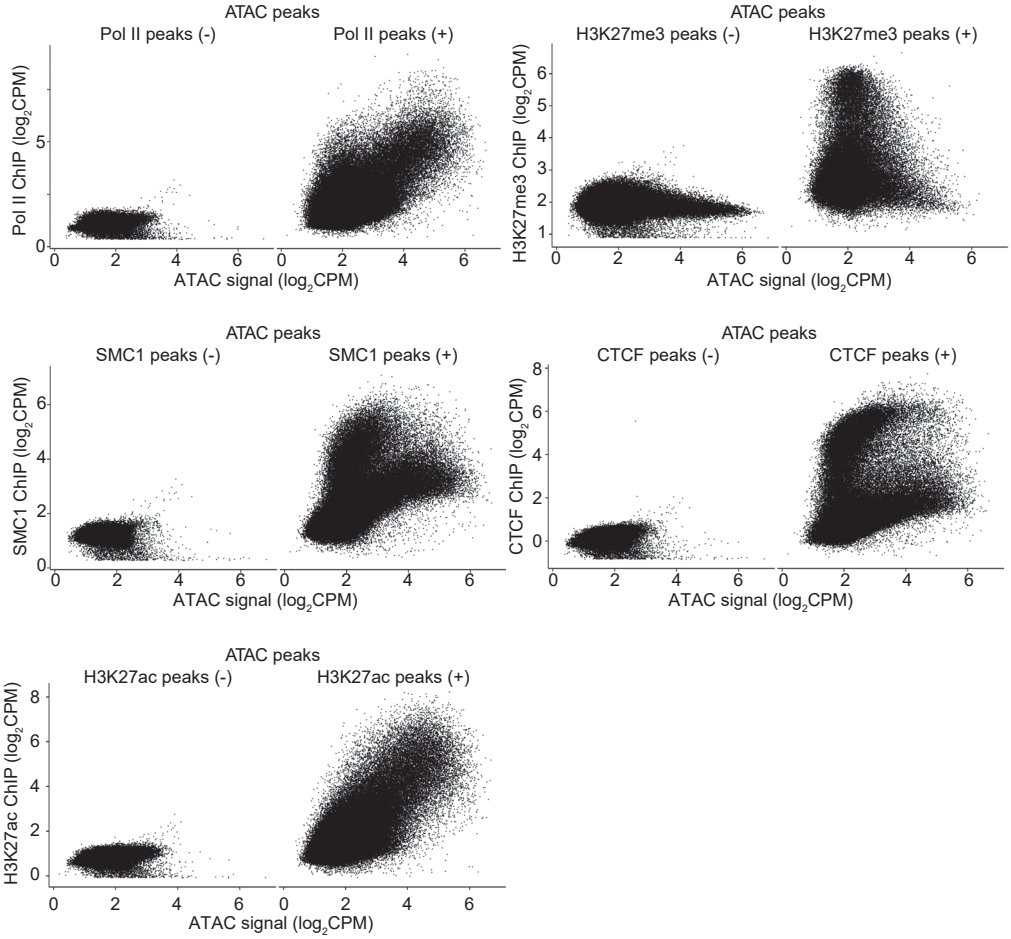

Supplementary Fig. 2 | Correlation between ATAC and ChIP signals. a. Correlation between ATAC and indicated ChIP intensities at each ATAC peak with or without overlapping ChIP-seq peaks.

Supplementary Fig. 3

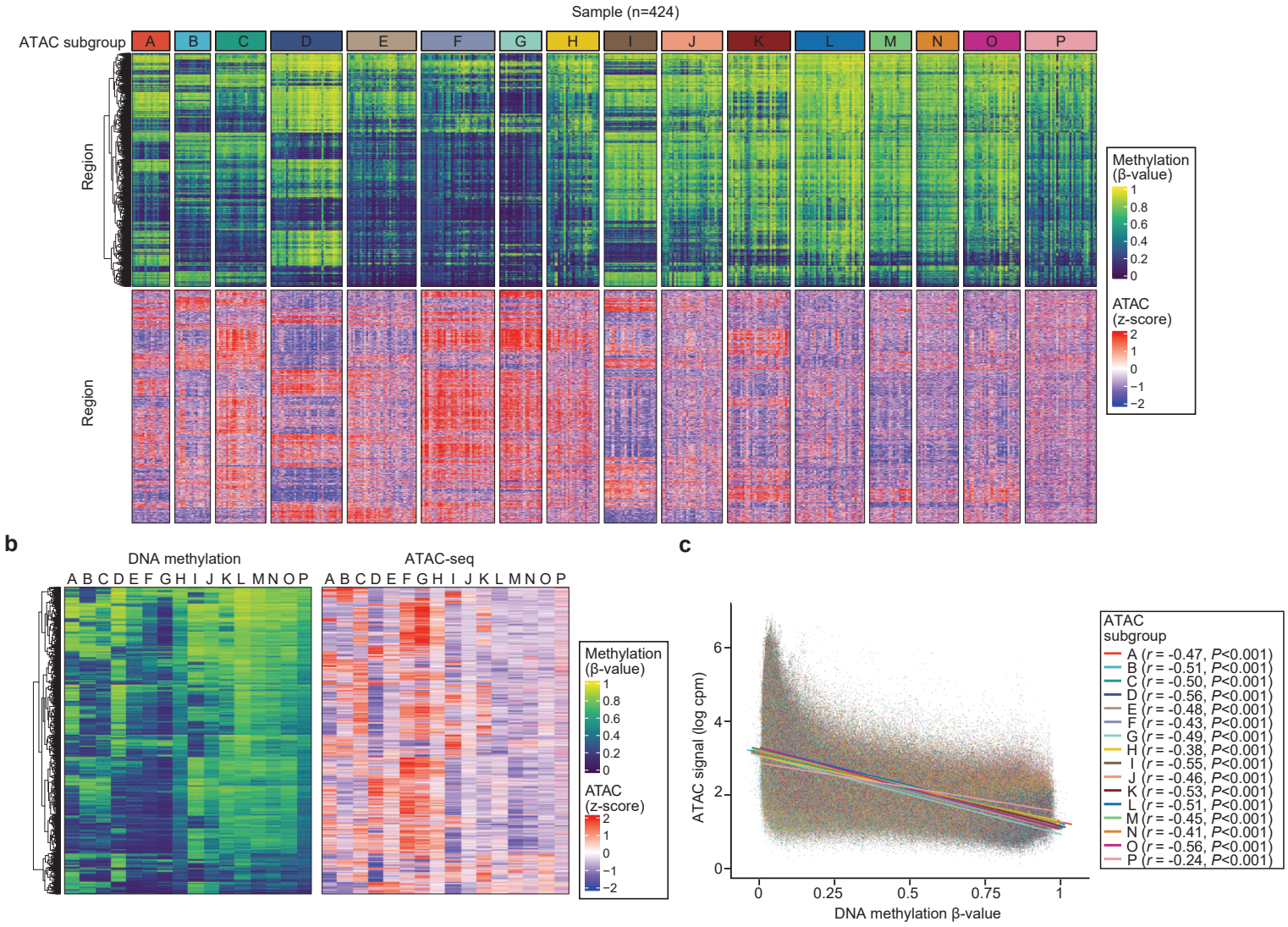

Supplementary Fig. 3 | Distinct DNA methylation profiles across subgroups. a. DNA methylation levels of 3,000 variable regions in each sample, grouped by ATAC subgroups. ATAC signals for the same regions in the same order are shown below. **b.** Mean DNA methylation levels of the 3,000 variable regions in each ATAC subgroup (left), and corresponding mean ATAC signals (right), aligned to the same regions in the same order. **c.** Correlation between DNA methylation and ATAC signals at the corresponding regions in each ATAC subgroup. *r* and *P* values were calculated using Pearson correlation.

Supplementary Fig. 4

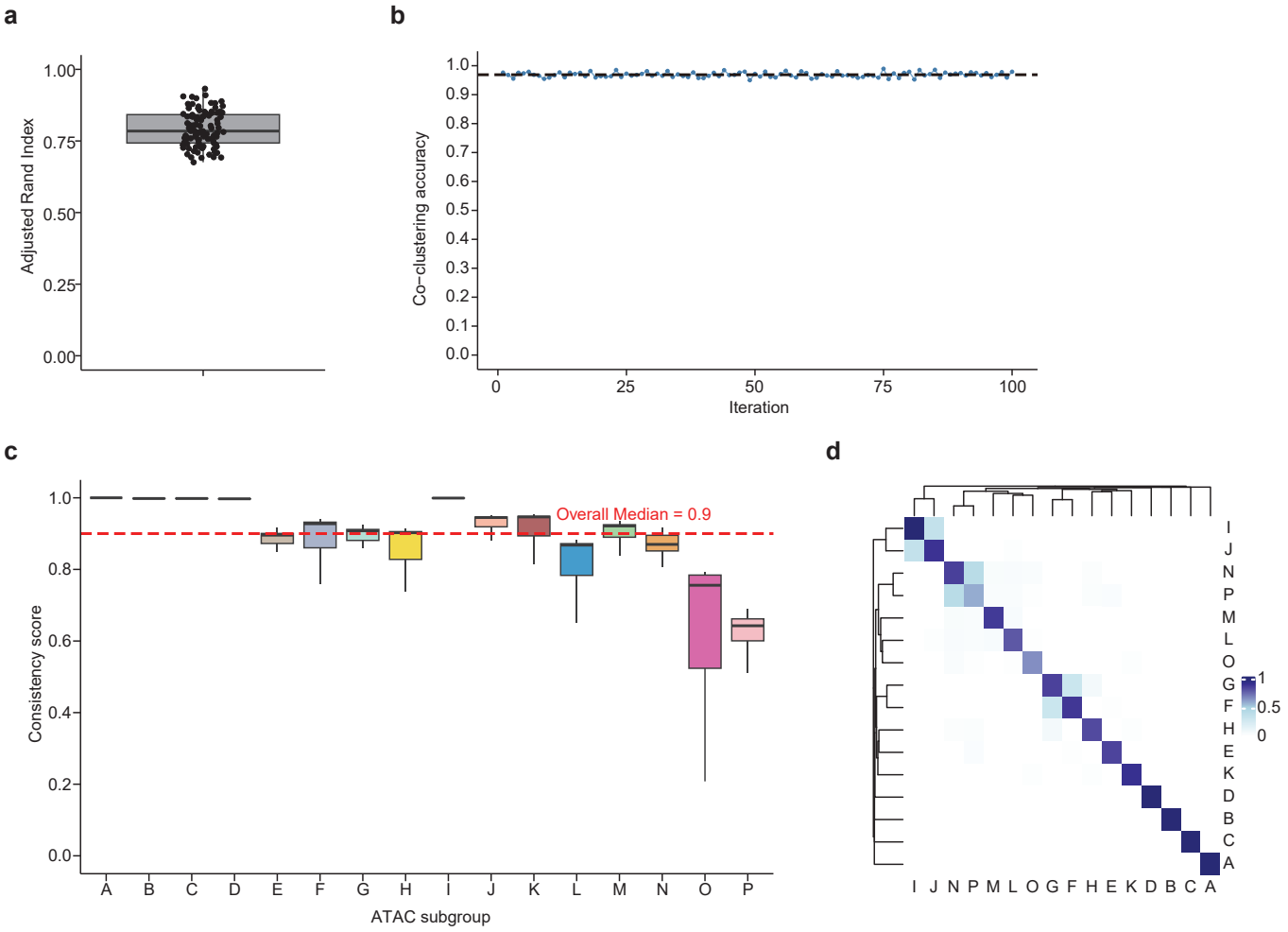

Supplementary Fig. 4 | Benchmark of ATAC-based clustering. a. Distribution of Adjusted Rand Index (ARI) values across 100 resampling iterations, quantifying the agreement between resampled and original clustering. **b.** Co-clustering accuracy per iteration, defined as the proportion of sample pairs for which both original and resampled cluster assignments agreed. **c.** Cluster-level stability, summarized as the distribution of sample-wise consistency scores. **d.** Cluster-cluster similarity matrix showing the mean co-occurrence frequency between each pair of original clusters.

Supplementary Fig. 5

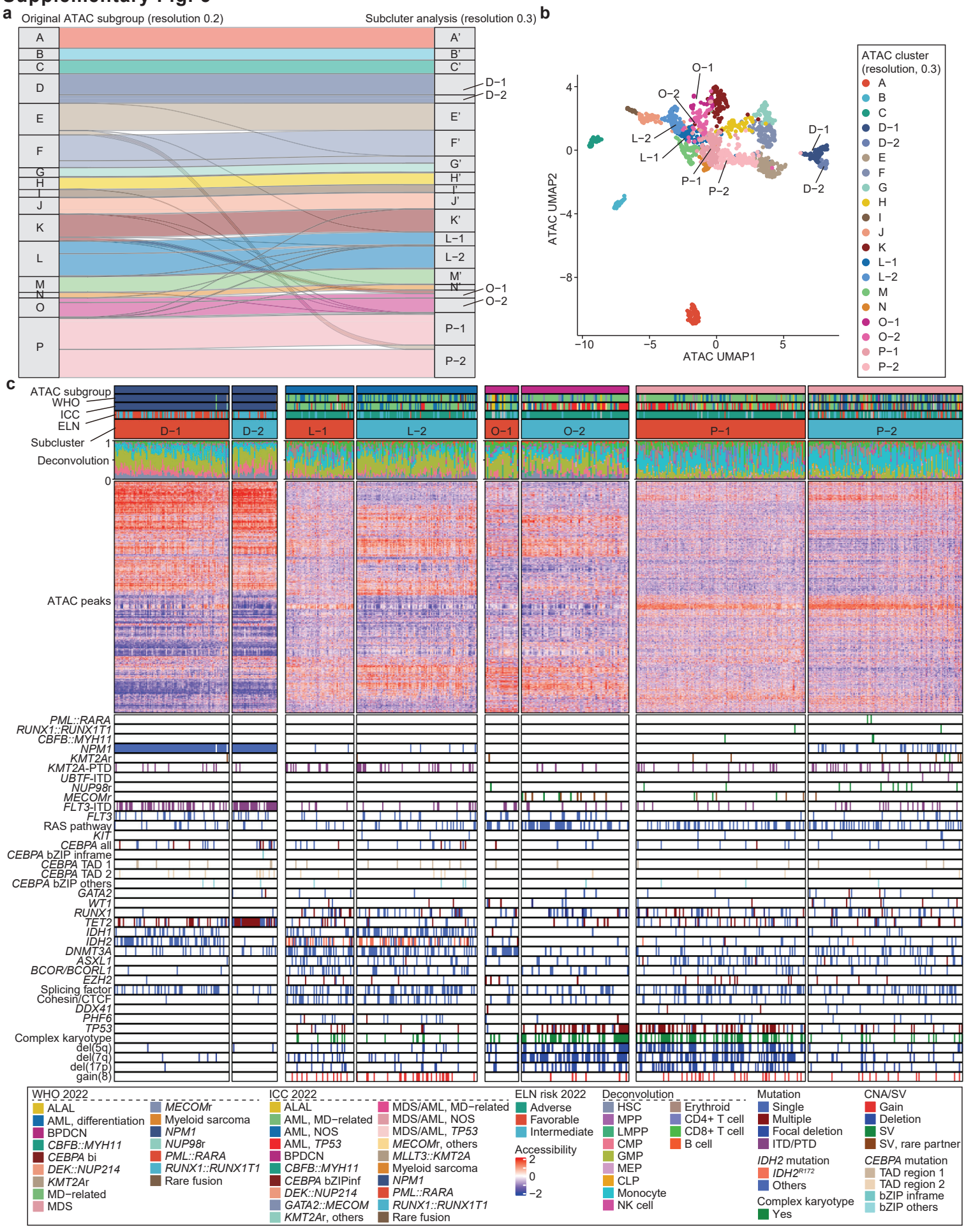

Supplementary Fig. 5 | Subclusters identified by high-resolution clustering based on ATAC-seq profiles. a. Sankey plot showing the mapping between ATAC clusters identified by Leiden clustering at an original resolution (0.2, original ATAC subgroups) and high-resolution (0.3). **b.** UMAP plot based on ATAC-seq profiles. Each dot represents each patient, and colors indicate ATAC clusters identified by Leiden clustering at a high-resolution (0.3). **c.** Summary of subclusters identified by a high-resolution clustering, with AML diagnosis, differentiation status inferred by CIBERSORTx software[27] using ATAC-seq data (deconvolution), scaled ATAC intensities on 3,000 variable ATAC peaks (same order with Fig. 1c), and genetic abnormalities. Each column represents each patient.

Supplementary Fig. 6

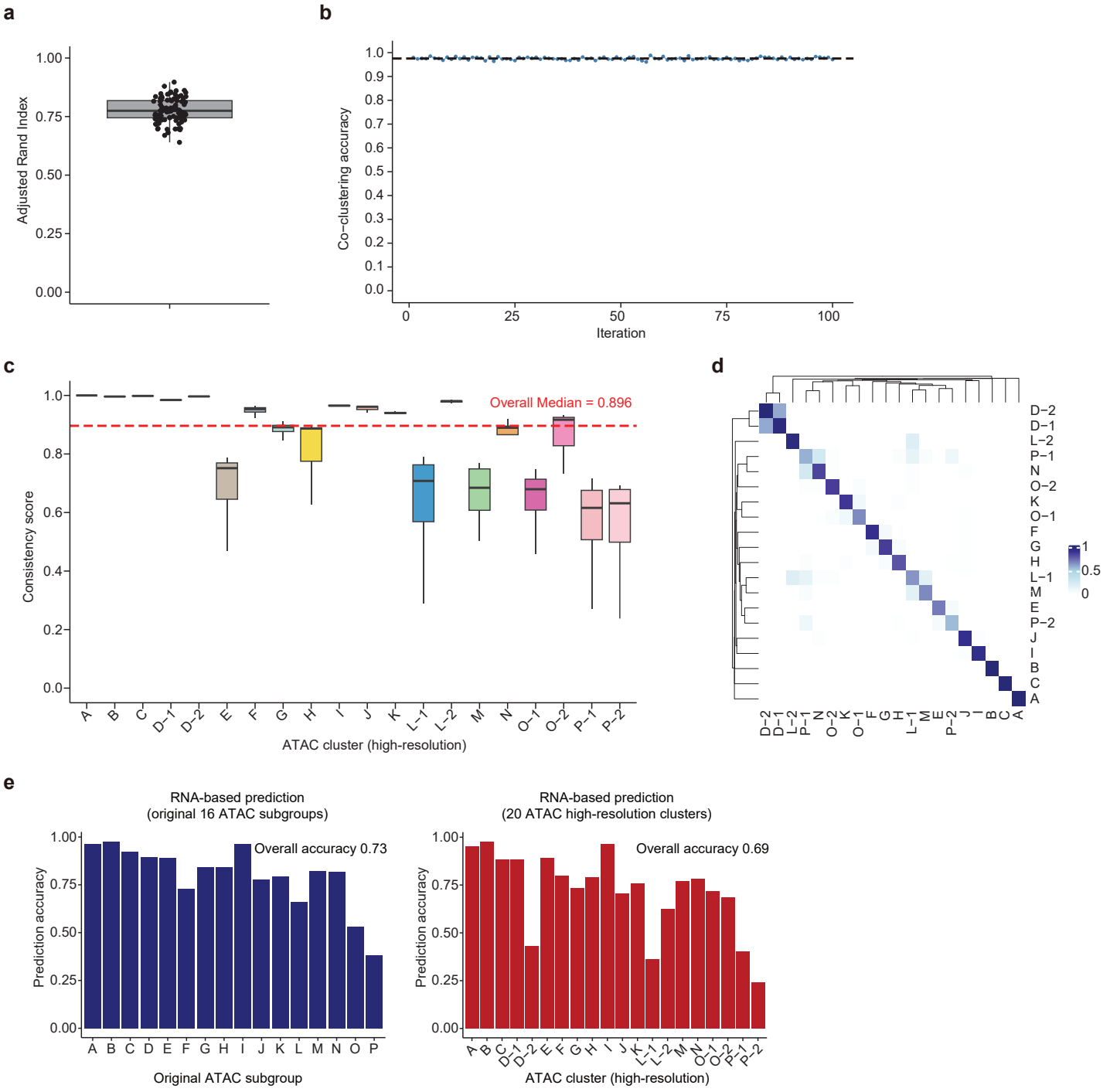

Supplementary Fig. 6 | Benchmark of ATAC-based high-resolution clustering. a. Distribution of Adjusted Rand Index (ARI) values across 100 resampling iterations, quantifying the agreement between resampled and original high-resolution clustering. **b.** Co-clustering accuracy per iteration, defined as the proportion of sample pairs for which both original and resampled cluster assignments agreed. **c.** Cluster-level stability, summarized as the distribution of sample-wise consistency scores. **d.** Cluster-cluster similarity matrix showing the mean co-occurrence frequency between each pair of original high-resolution clusters. **e.** Prediction accuracy of expression-based models for each ATAC subgroup (left) and ATAC cluster identified with high-resolution clustering (right). The models were built using the Classification to Nearest Centroids (ClaNC) algorithm[30], a nearest centroid classifier, which ranks genes by standard t-statistics and selects subgroup-specific genes. Fifteen genes per subgroup were selected and incorporated into the prediction model. The accuracy of prediction models was calculated by the 5-fold cross validation, separating 80% of samples for training and the remaining 20% for validation.

Supplementary Fig. 7

a

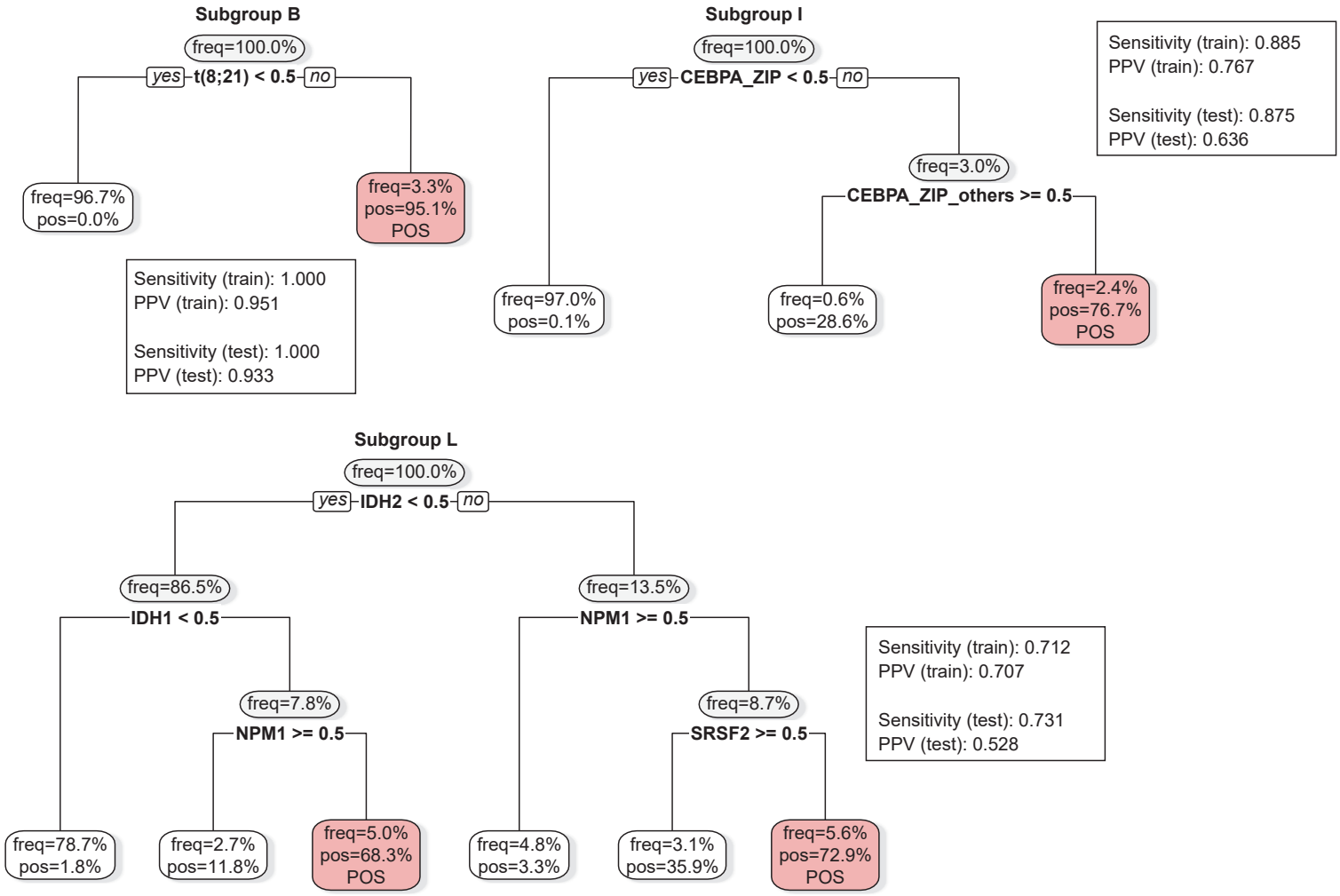

b

Performance summary (maxdepth=3)

Subgroup	Internal splits	Sensitivity	PPV	F1−score	Balanced accuracy
A	1	1.00	1.00	1.00	1.00
B	1	1.00	0.93	0.97	1.00
C	1	0.92	0.86	0.89	0.96
D	3	0.27	0.55	0.36	0.63
E	3	0.18	0.83	0.29	0.59
F	2	0.03	0.50	0.06	0.52
G	3	0.17	0.50	0.25	0.58
H	0	0.00	NA	NA	0.50
I	2	0.88	0.64	0.74	0.93
J	3	0.42	1.00	0.59	0.71
K	3	0.08	0.67	0.14	0.54
L	5	0.73	0.53	0.61	0.84
M	1	0.71	0.77	0.74	0.85
N	3	0.00	0.00	NA	0.50
O	2	0.00	0.00	NA	0.50
P	5	0.07	0.33	0.12	0.52

Value: 1.0, 0.5, 0.0

Supplementary Fig. 7 (continued)

c

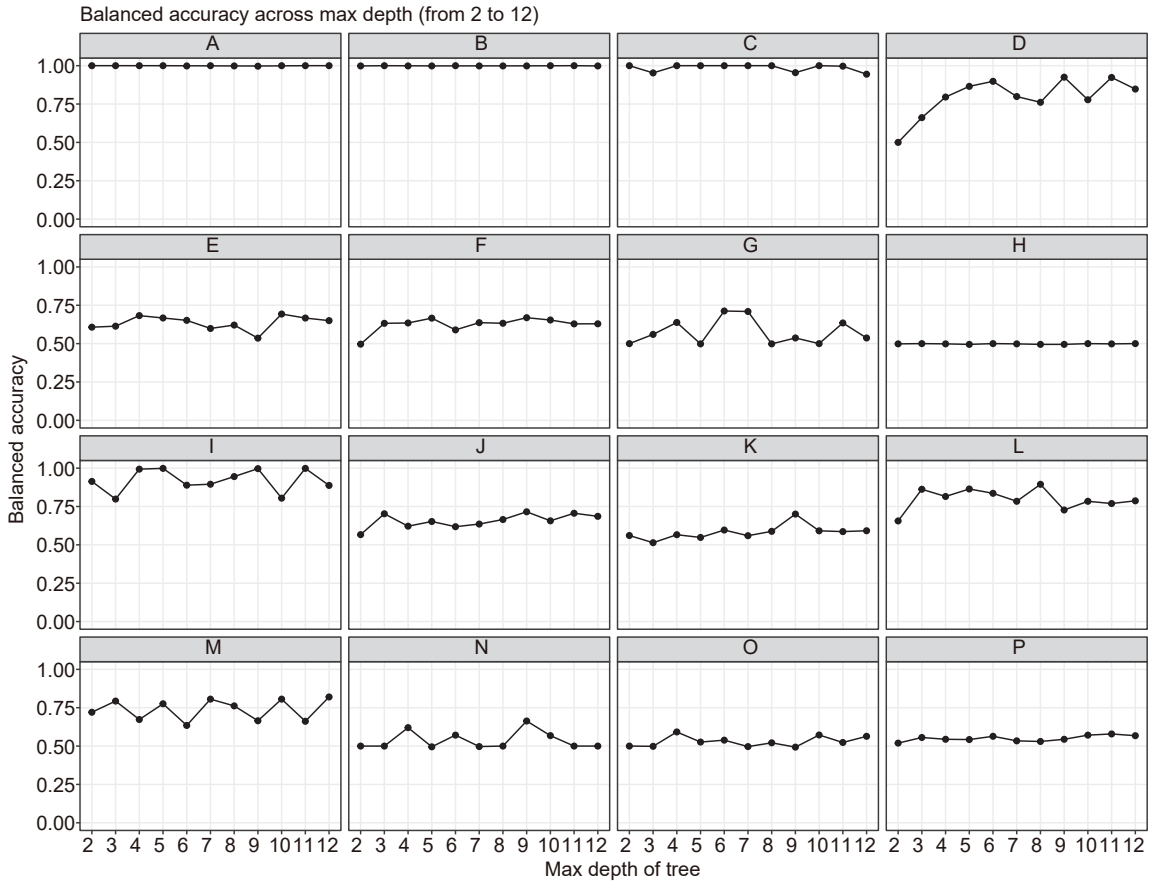

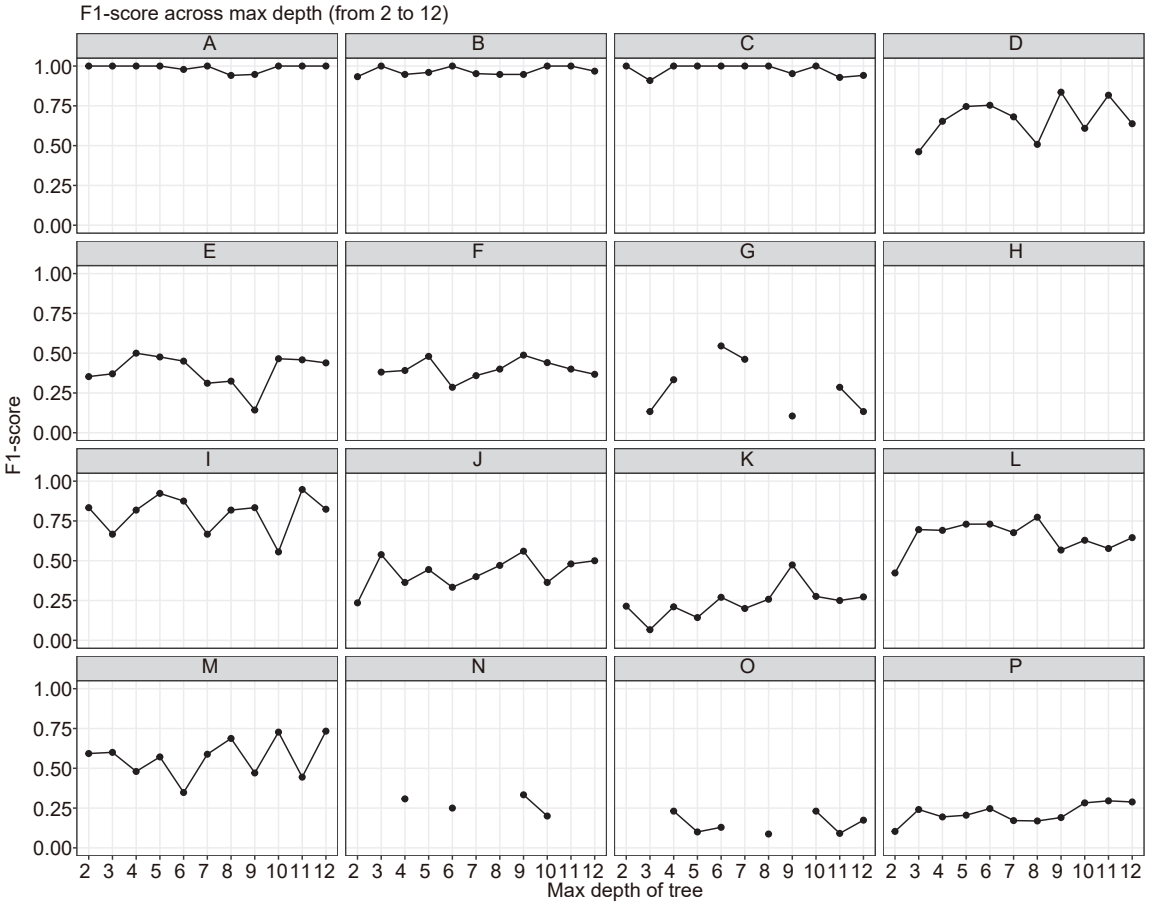

Supplementary Fig. 7 | Genome-based decision tree analysis of ATAC subgroups. a. Representative genome-based decision trees for ATAC subgroups. Genome-based decision tree classifiers were constructed to assess whether ATAC-defined subgroups can be predicted from genomic alterations. For each ATAC subgroup (A–P), a binary one-versus-rest classifier was trained using gene mutations, CNAs, and structural variants as binary input features. Models were trained using a CART framework, with samples randomly split into training (80%) and test (20%) sets. Example decision trees are shown for ATAC subgroups with relatively higher predictability (subgroups B, I, and L), with the maximum tree depth fixed at 3. Internal nodes indicate genomic features used for splitting, with thresholds representing presence (≥0.5) or absence (<0.5) of the alteration. At each node, *freq* denotes the proportion of samples reaching that node, and *pos* denotes the proportion of samples belonging to the target subgroup. Terminal nodes labeled "POS" represent leaves classified as the positive class. Sensitivity and positive predictive value (PPV) are reported for both training and test sets. Except for Subgroup B, which is expected to be predictable based on known defining alterations, even relatively well-performing subgroups show only modest sensitivity and/or PPV, indicating limited identification by genome-based rules. **b.** A summary matrix shows model complexity and predictive performance for each ATAC subgroup. The leftmost column indicates the number of internal splits in the final tree, reflecting model complexity, and the remaining columns show sensitivity, PPV, F1-score, and balanced accuracy evaluated on the test set. Balanced accuracy is defined as the mean of sensitivity and specificity and accounts for class imbalance, whereas the F1-score represents the harmonic mean of sensitivity and PPV. Overall, only a small number of subgroups achieve high performance with shallow trees, highlighting the limited predictability of most ATAC subgroups using genome-based rules. **c.** Balanced accuracy (top) and F1-score (bottom) are plotted as a function of increasing maximum tree depth (2–12) for each ATAC subgroup. Increasing model complexity yields only marginal performance gains for most subgroups, indicating that deeper trees do not substantially improve subgroup prediction.

Supplementary Fig. 8

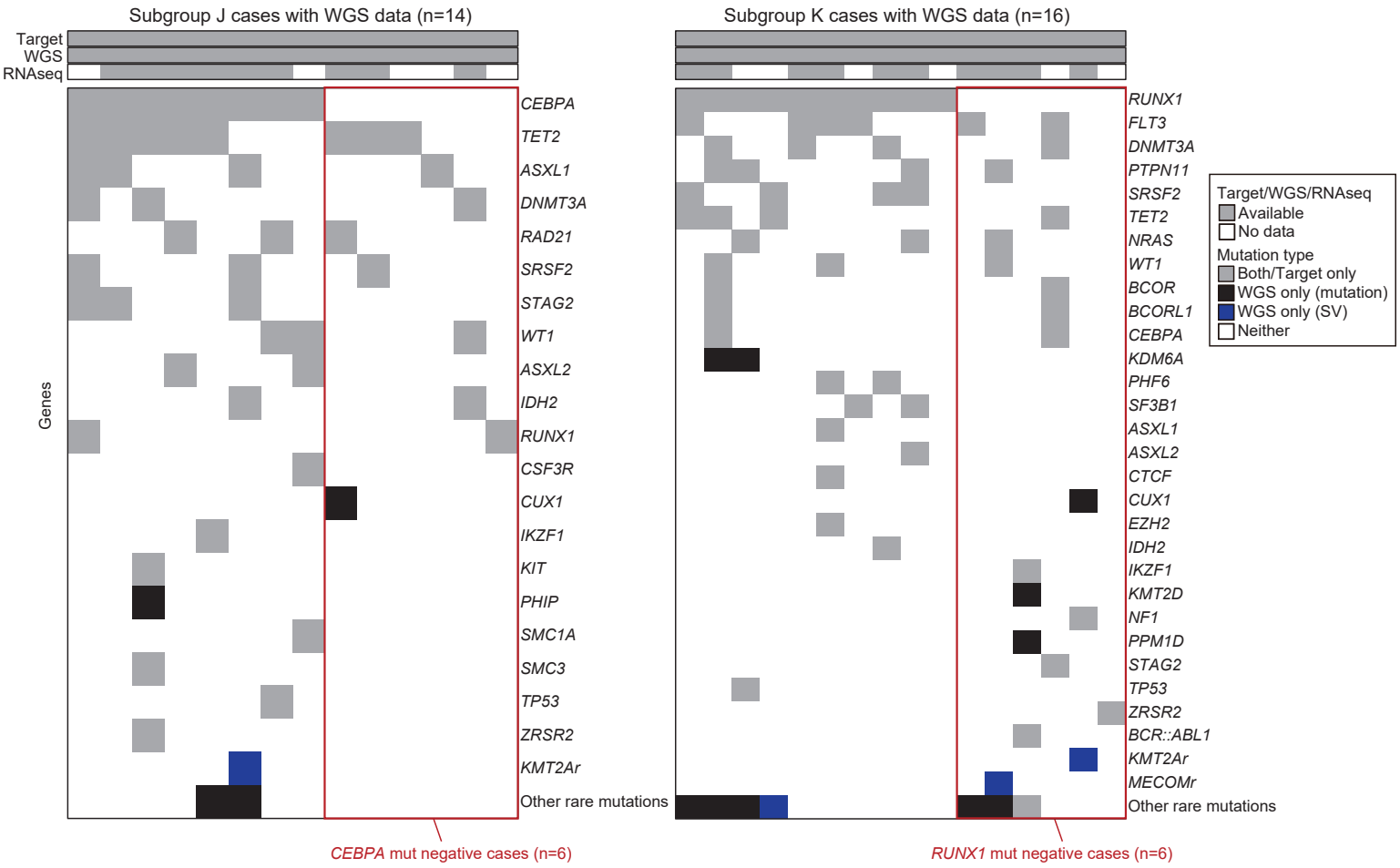

Supplementary Fig. 8 | WGS-based systematic genomic analysis in ATAC subgroups. Summary of all gene alterations found in subgroup J and K with available WGS data. In the WGS analysis, both known and previously unknown genetic alterations were included. Gene alterations detected by targeted-capture sequencing are shown in gray, whereas those identified only by WGS (but not by targeted-capture sequencing) are highlighted in other colors. Data types obtained for each sample are indicated in gray at the top of the heatmap.

Supplementary Fig. 9

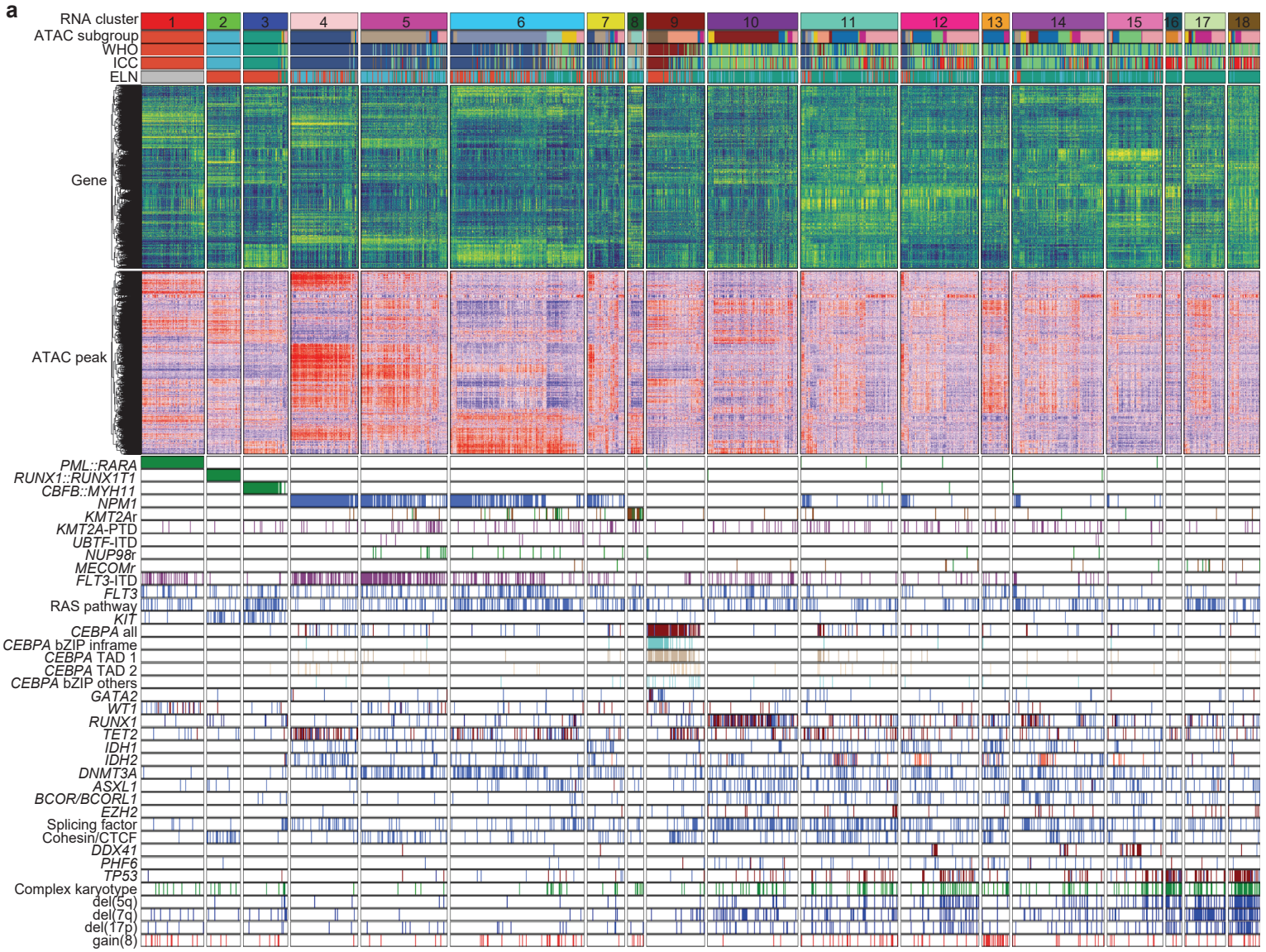

Supplementary Fig. 9 | RNA-based clustering. a. Summary of RNA-based clusters with AML diagnosis, differentiation status inferred by CIBERSORTx software[27] using ATAC-seq data (deconvolution), scaled RNA/ATAC expression levels on 3,000 variable genes/ATAC peaks, and genetic abnormalities. Each column represents each patient. **b.** Sankey plot showing the mapping between ATAC subgroups and RNA clusters.

Supplementary Fig. 10

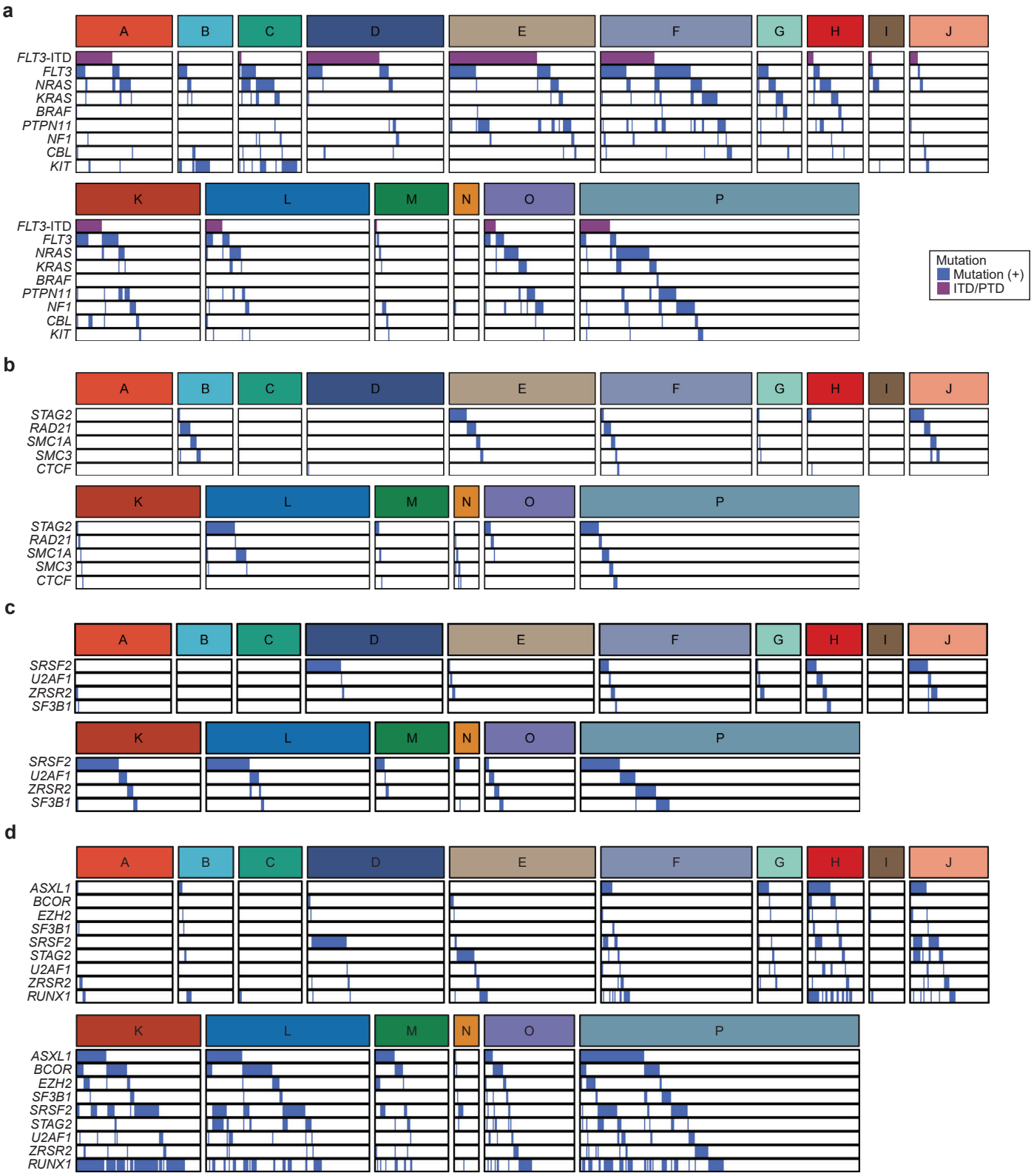

Supplementary Fig. 10| Distribution of functionally categorized driver mutations across subgroups. a-d. Summary of RAS and related signaling pathway (**a**), cohesin complex (**b**), splicing factor (**c**), and MDS-related mutations (**d**) in each subgroup. Column represents patients, sorted by the presence of indicated genetic abnormalities. In **Fig. 1c**, RAS pathway mutations (*NRAS*, *KRAS*, *PTPN11*, *CBL*, *NF1*, and *BRAF*), cohesin complex (*STAG2*, *RAD21*, *SMC1A*, *SMC3*, and *CTCF*), and splicing factor (*SRSF2*, *U2AF1*, *ZRSR2*, and *SF3B1*) mutations are grouped.

Supplementary Fig. 11

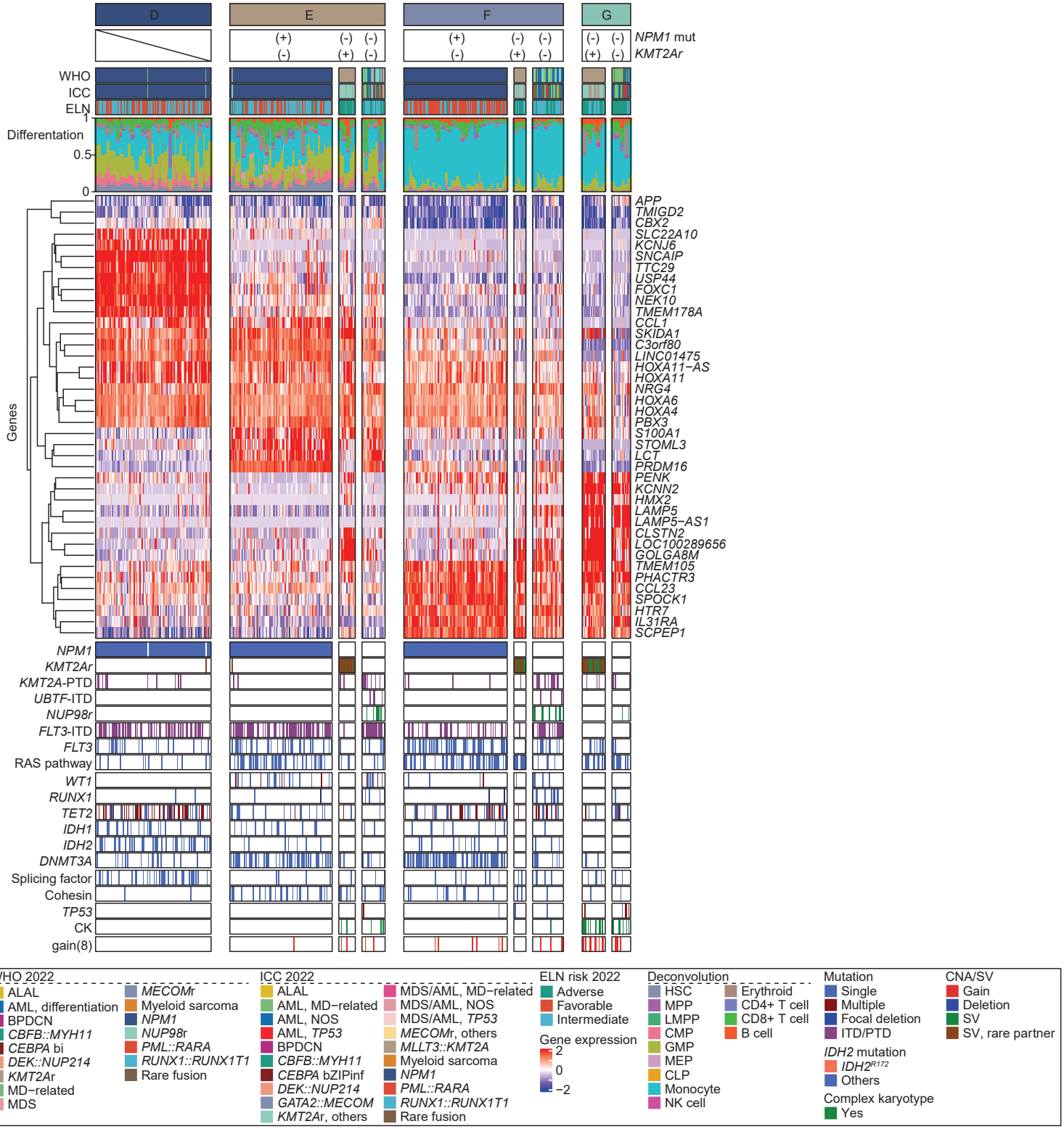

Supplementary Fig. 11 | Summary of HOX-related subgroups. Summary of HOX-related subgroups according to driver mutations, such as *NPM1* mutations or *KMT2Ar*, with AML diagnoses, estimated differentiation status, normalized expression of representative genes, and genetic abnormalities. Each column represents one patient.

Supplementary Data Fig. 12

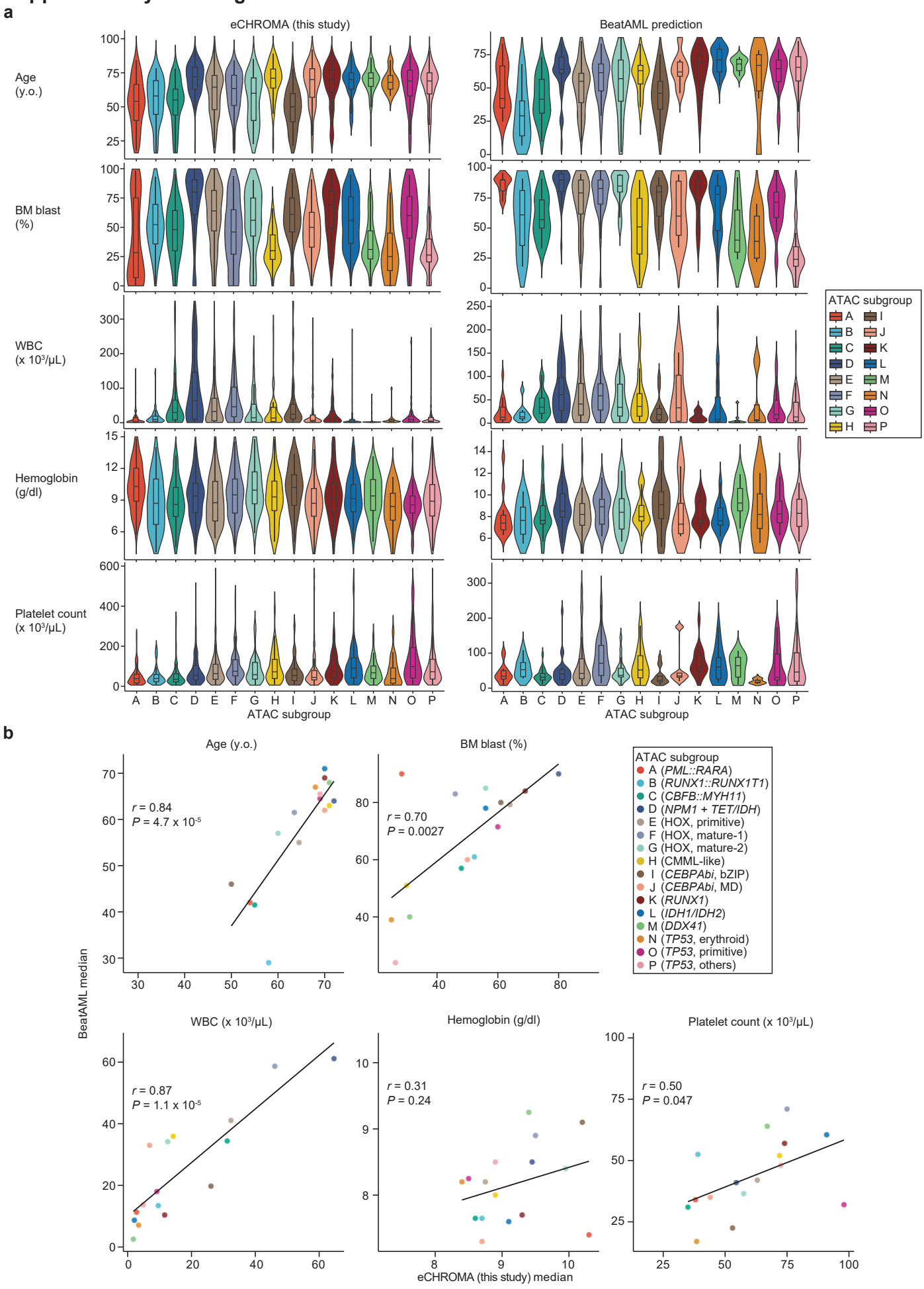

Supplementary Fig. 12| Summary of clinical parameters in ATAC subgroups. a. Clinical parameters for ATAC subgroups in our cohort and predicted ATAC subgroups in the BeatAML cohort. For box plots, the center line indicates the median, the box limits indicate the upper and lower quartiles, and the whiskers extend to the minimum and maximum values within 1.5× IQR. **b.** Median values of clinical parameters for ATAC subgroups in our dataset (x-axis) and for predicted ATAC subgroups in the BeatAML dataset (y-axis). *r* and two-sided *P* values were calculated using Pearson correlation.

Supplementary Fig. 13

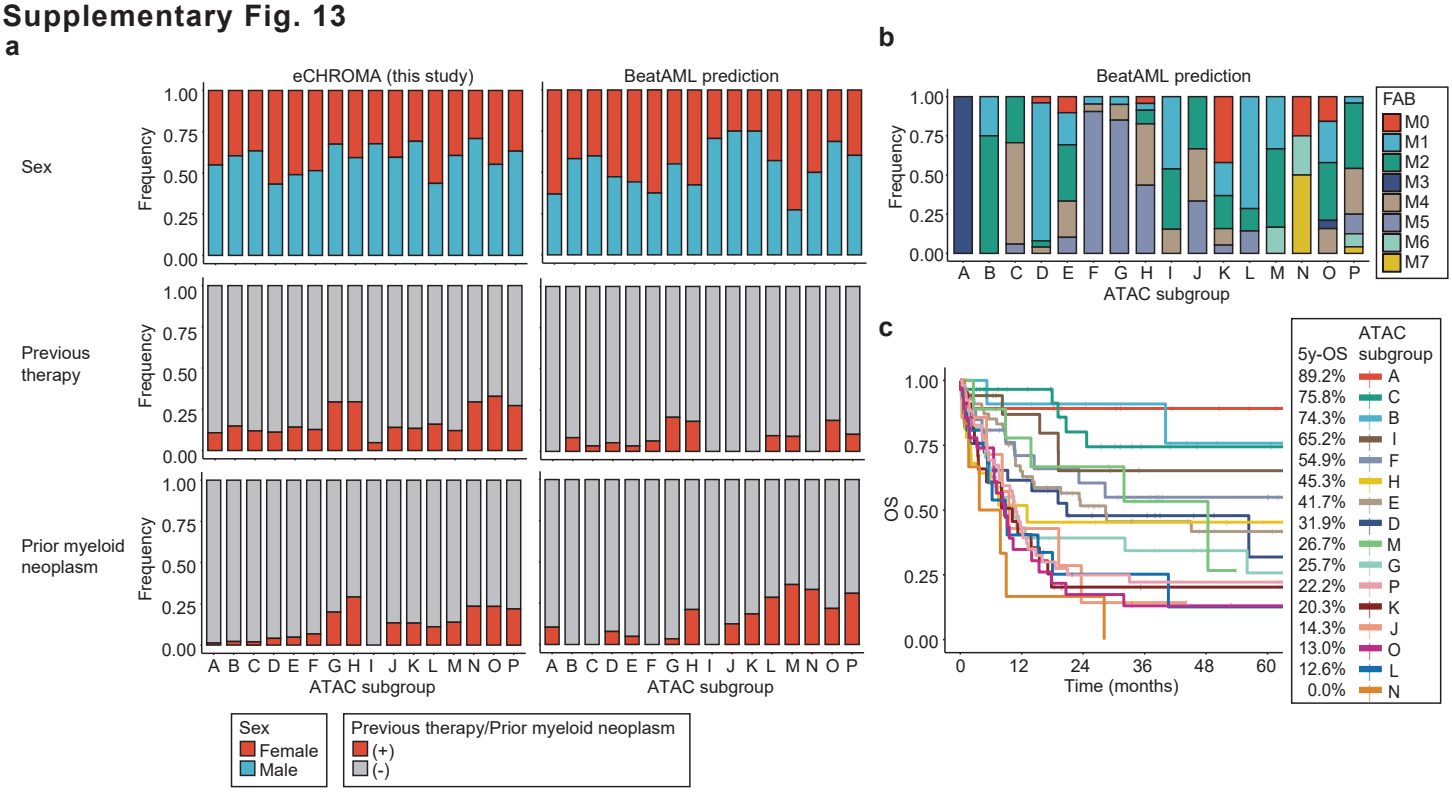

Supplementary Fig. 13 | Clinical features of ATAC subgroups. a. Clinical features for ATAC subgroups in our cohort and predicted ATAC subgroups in the BeatAML cohort. **b.** Proportion of each FAB diagnosis in predicted ATAC subgroups in the BeatAML cohort. **c.** Kaplan–Meier survival curves for OS of patients who received intensive chemotherapy in the BeatAML dataset, categorized by predicted ATAC subgroups.

Supplementary Fig. 14

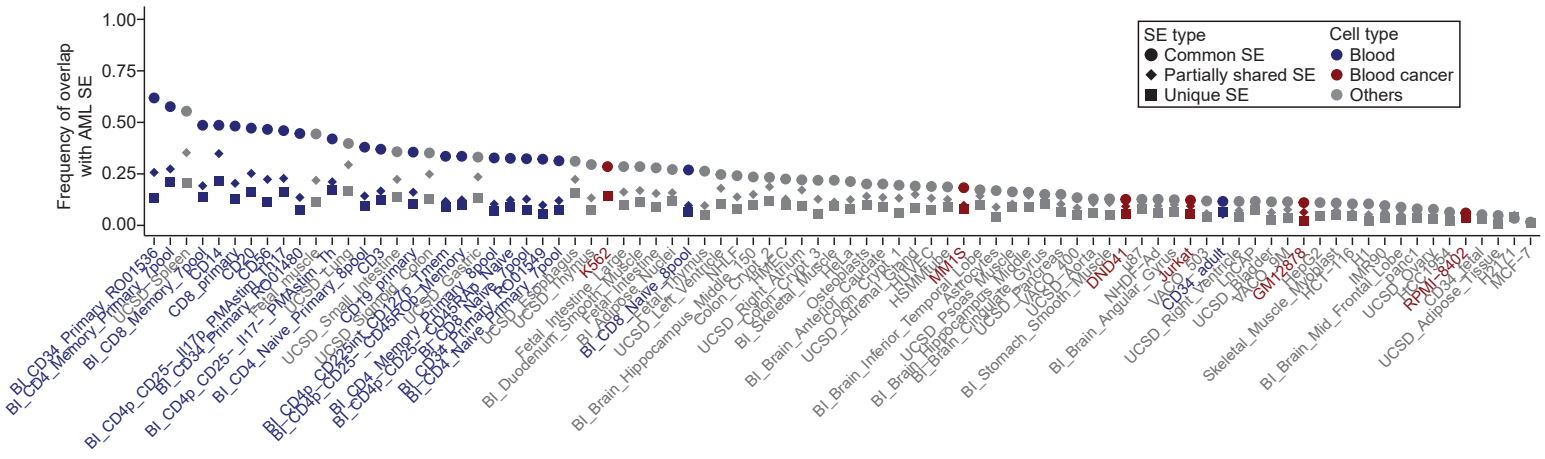

Supplementary Fig. 14 | Distribution of AML SEs across cell types and cancers. Frequency of overlapped SEs from various cell types and cancers reported in a previous study[34] with common, partially shared, and unique SEs of AML (Fig. 2c).

Supplementary Fig. 15

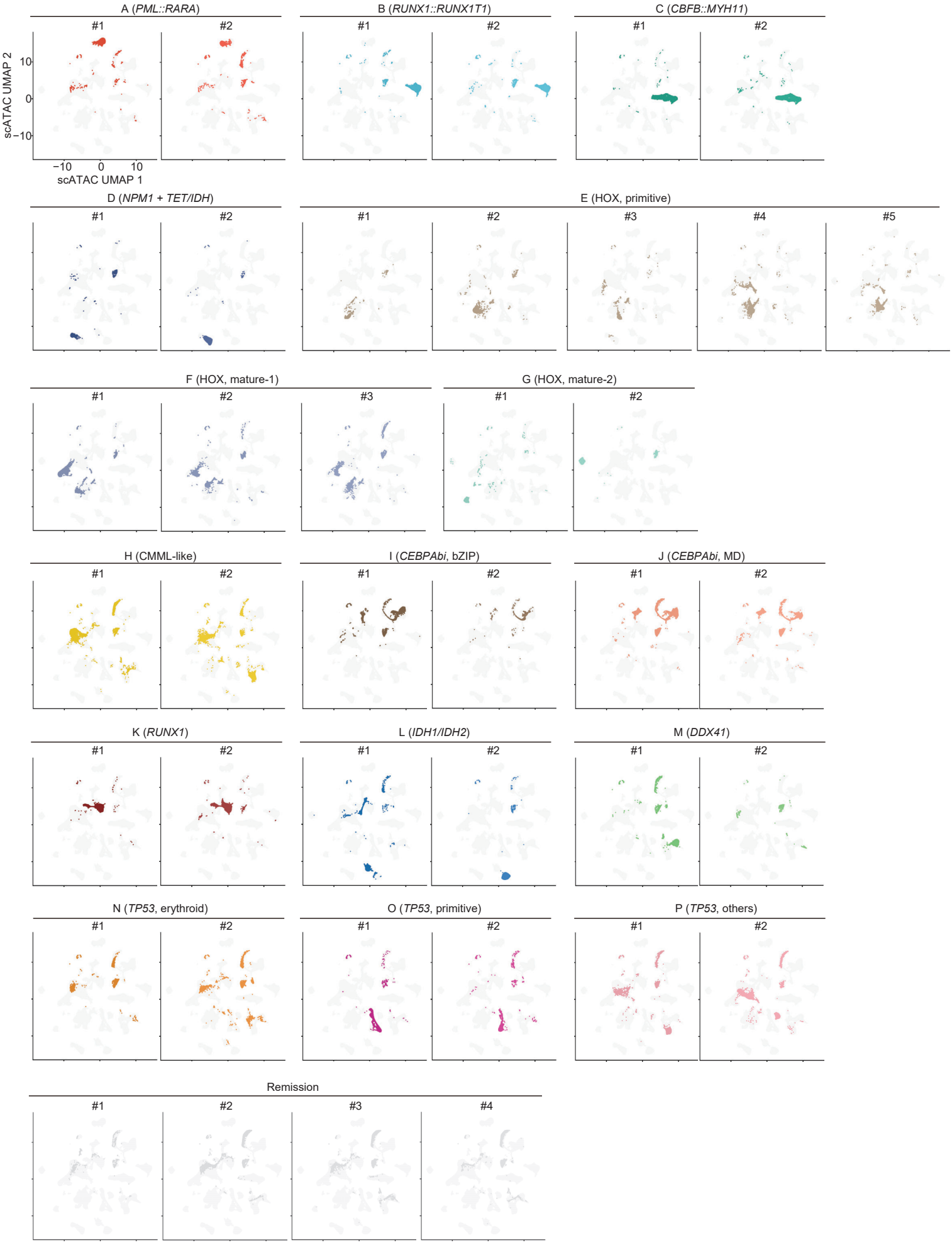

Supplementary Fig. 15 | scATAC-seq profiles for individual patient samples. UMAP plots based on scATAC-seq profiles for each patient sample, indicated by color.

Supplementary Fig. 16

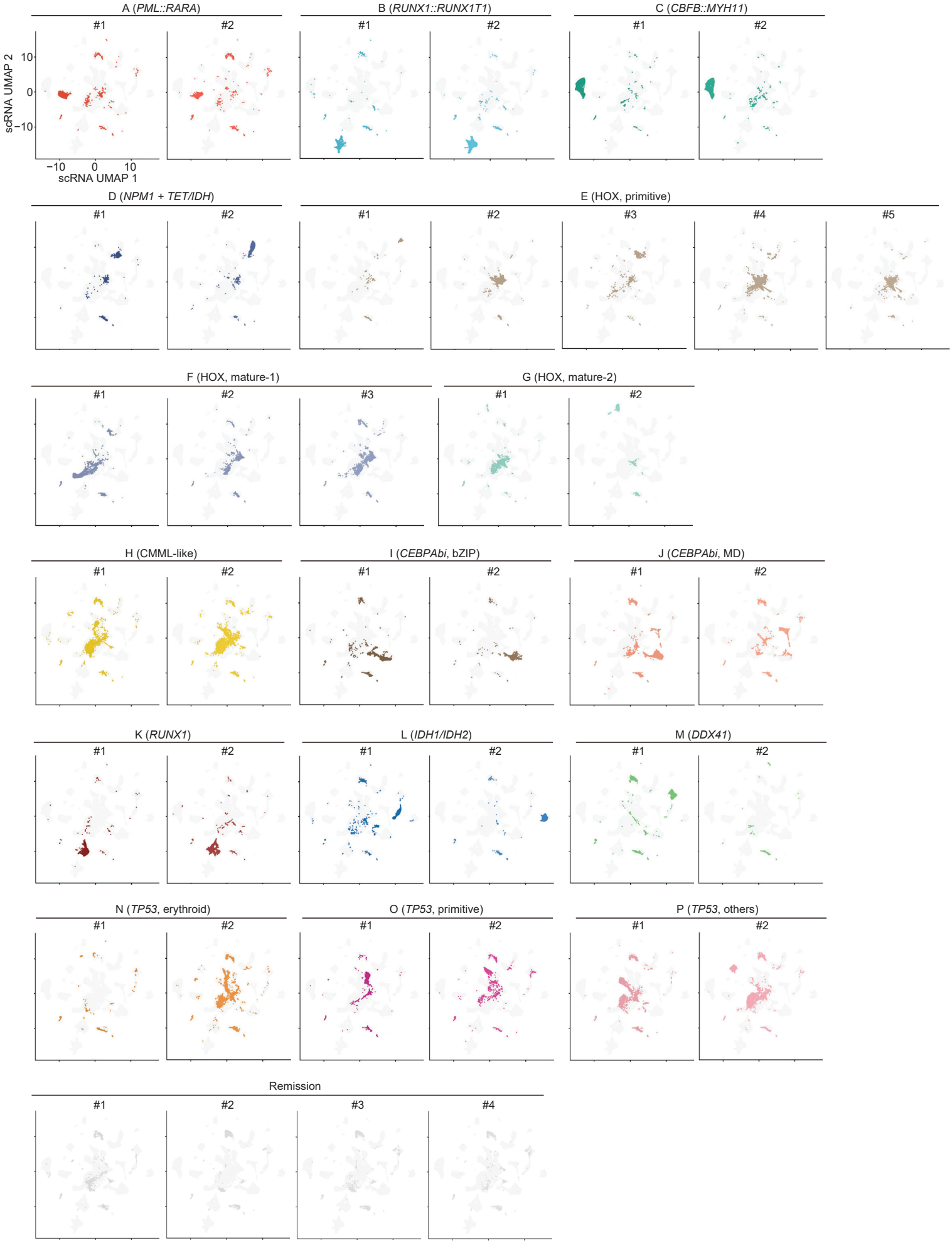

Supplementary Fig. 16 | scRNA-seq profiles for individual patient samples. UMAP plots based on scRNA-seq profiles for each patient sample, indicated by color.

Supplementary Fig. 17

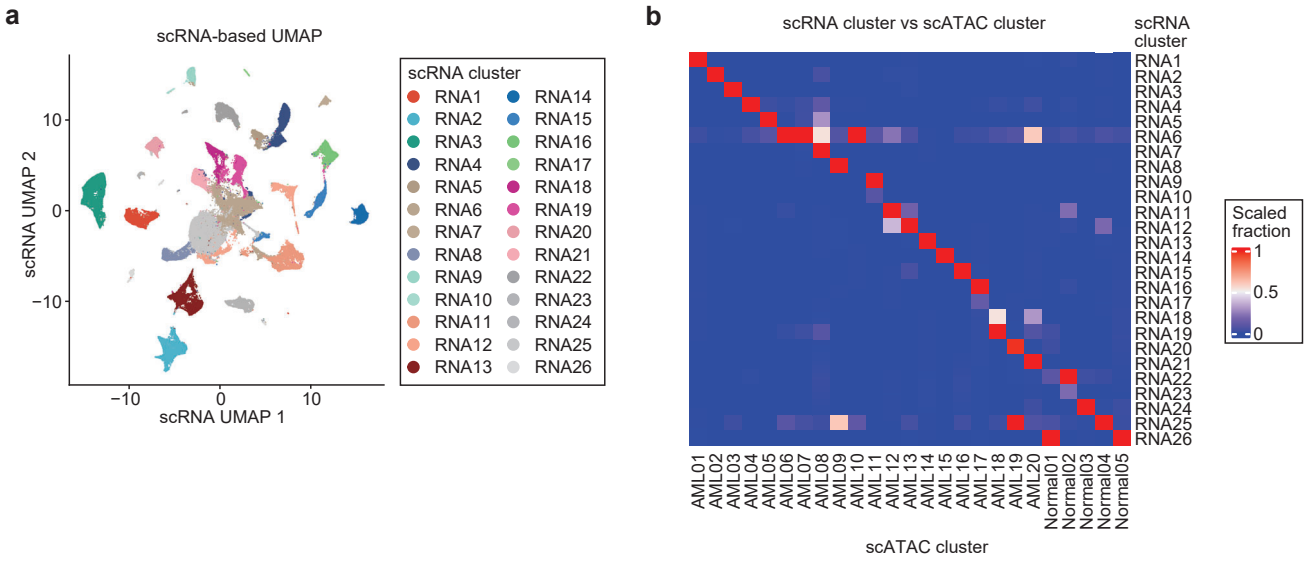

Supplementary Fig. 17 | scATAC- and scRNA-based clusters. a. UMAP plot based on scRNA-seq profiles. Each dot represents one cell, colored by scRNA-based clusters. **b.** Cluster residence heatmaps, showing the percentage of cells from each scATAC cluster residing within each scRNA-based cluster.

Supplementary Fig. 18

Supplementary Fig. 18 | Differentiation states of AML cells from individual patient samples. UMAP plots of AML cells from each patient sample, indicated by color, mapped to the reference scRNA-seq UMAP, derived from previous scRNA-seq dataset of normal human hematopoiesis[41].

Supplementary Fig. 19

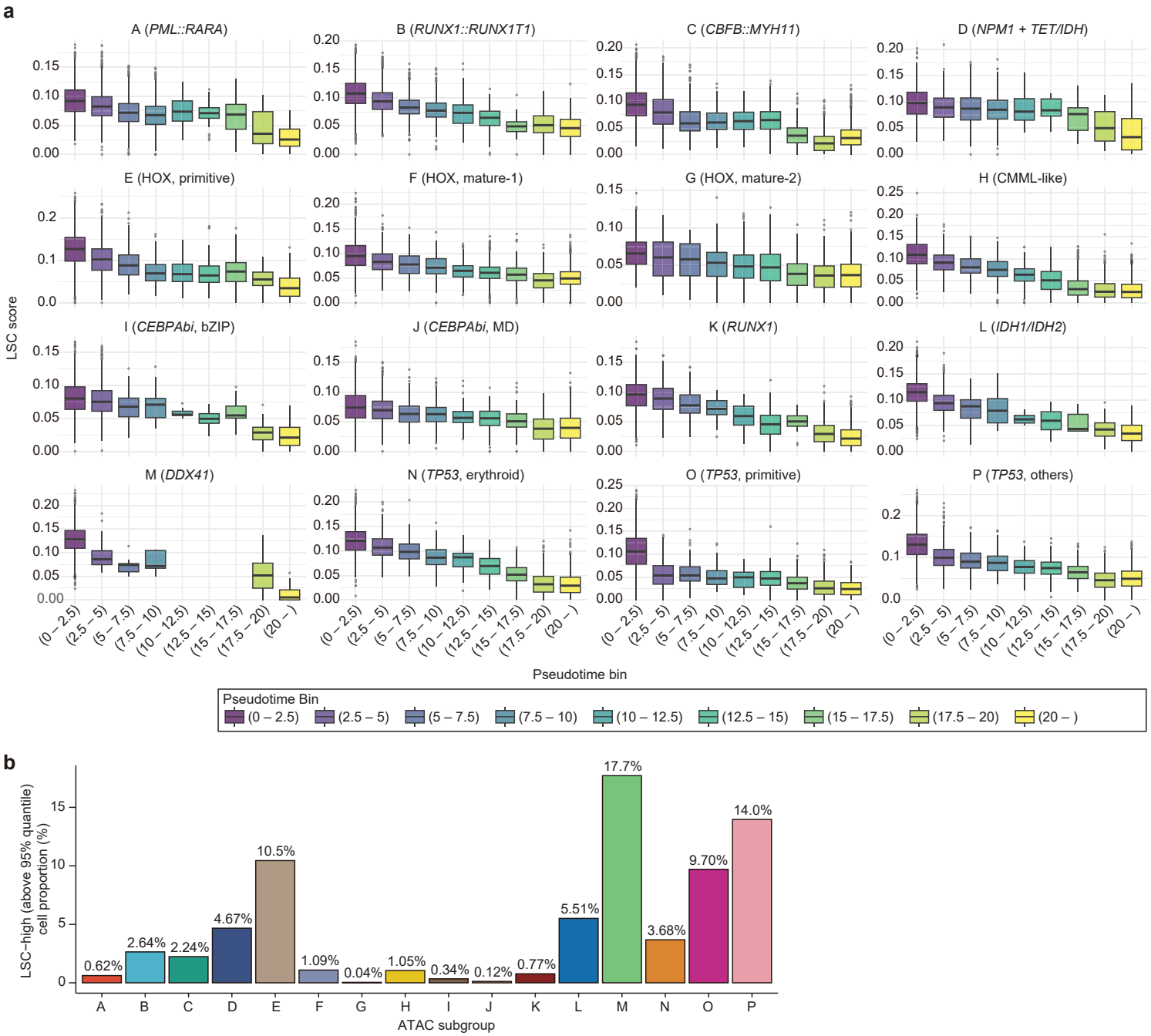

Supplementary Fig. 19 | Leukemia stem cell (LSC) scores at the single-cell level. a. Distribution of LSC scores across pseudotime bins along the myeloid differentiation trajectory in each ATAC subgroup. **b.** Proportion of cells with high LSC scores (above 95% quantile) in each ATAC subgroup.

Supplementary Fig. 20

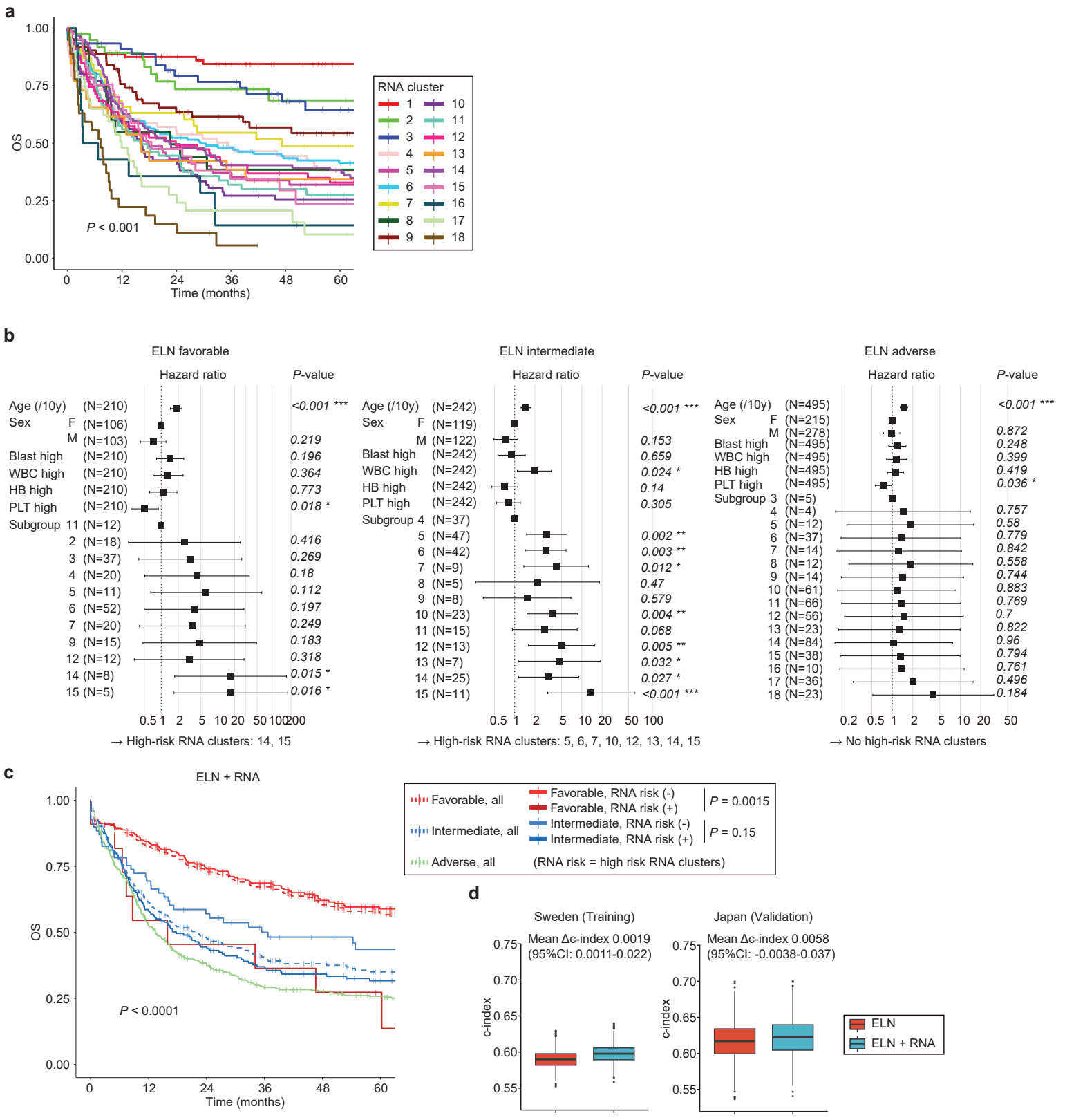

Supplementary Fig. 20 | Prognostic impact of RNA-based clusters. a. Kaplan–Meier survival curves for OS of patients who received intensive chemotherapy, categorized by RNA clusters. *P* value was calculated using the log-rank test. **b.** Cox regression analysis for patients in each ELN risk group, incorporating clinical variables and RNA clusters with more than two patients. In each analysis, the RNA cluster with the most favorable survival was used as the reference, and high-risk RNA clusters were defined as those with significantly worse prognosis: RNA clusters 14 and 15 for ELN favorable, and clusters 5, 6, 7, 10, 12, 13, 14, and 15 for ELN intermediate. For ELN adverse risk, no high-risk RNA clusters were found. **c.** Kaplan–Meier survival curves for OS of patients who received intensive chemotherapy, categorized by the combined model of ELN and RNA. *P* value was calculated using the log-rank test. In the combined model, patients in ELN risk category favorable or intermediate were further stratified into two groups based on membership in high-risk RNA clusters, determined as shown in **b**. **d.** Estimates of the concordance index (c-index) derived from ELN and the combined model of ELN and RNA (as shown in panel **c**), using bootstrapping 1,000 times. The combined model was trained in the training (Swedish) cohort and evaluated in both training and validation (Japan) cohorts.

Supplementary Fig. 21

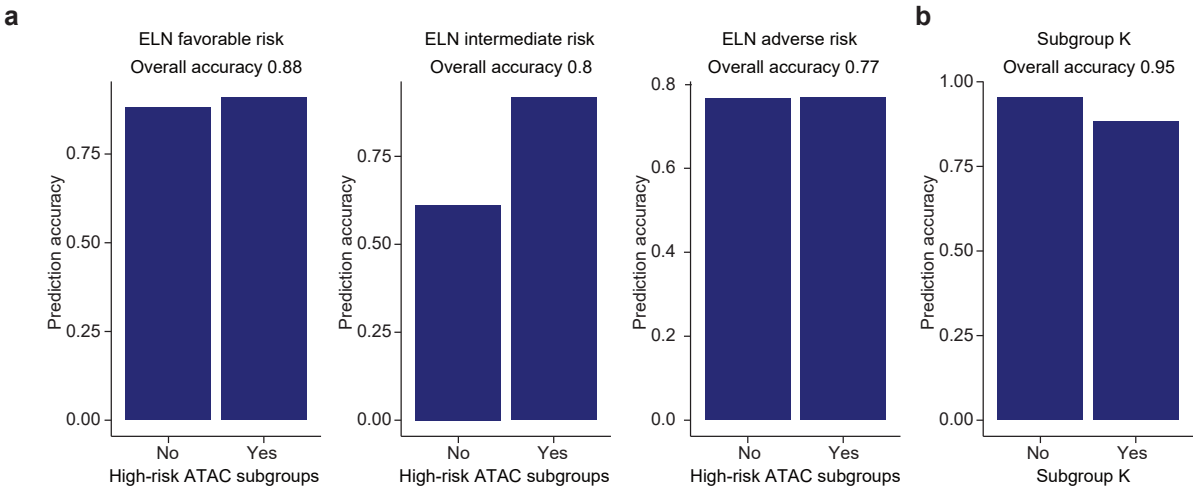

Supplementary Fig. 21 | Prediction of high-risk ATAC subgroups and subgroup K based on gene expression. a-b. Prediction accuracy of expression-based models for high-risk ATAC subgroups within each ELN risk group (**a**) or subgroup K (**b**), built using the Classification to Nearest Centroids (ClaNC) algorithm[30], a nearest centroid classifier, which ranks genes by standard t-statistics and selects subgroup-specific genes. Fifteen genes per group (a total of 30 genes per model) were selected and incorporated into the prediction model. The accuracy of prediction models was calculated by the 5-fold cross validation, separating 80% of samples for training and the remaining 20% for validation. In panel **a**, the models were trained to predict whether each sample belonged to one of the predefined high-risk ATAC subgroups. High-risk ATAC subgroups for each ELN risk category were defined as shown in Extended Data Fig. 9b: subgroup E for ELN favorable; subgroups E, F, G, K, L, and M for ELN intermediate; and subgroups D, E, G, O, and P for ELN adverse.

Supplementary Tables

Supplementary Table 1. Clinical characteristics of patients included in this study
Clinical characteristics of AML patients stratified by cohort. Continuous variables are presented as median (range), and categorical variables as number (percentage). *P*-values were calculated using the Wilcoxon rank-sum test for continuous variables and Fisher's exact test for categorical variables.

Supplementary Table 2. Diagnostic classification of AML patients
Distribution of AML diagnoses according to the WHO, ICC, and ELN classifications stratified by cohort. Values are shown as number (percentage) of patients within each diagnostic category.

Supplementary Table 3. Summary of analyzed AML samples
Sample-level metadata for AML cases included in this study. Information includes sample identifiers and availability of multi-omics data.

Supplementary Table 4. Gene targets included in the targeted-capture sequencing panel
List of genes included in the targeted-capture sequencing panel used for mutation analysis. The panel covers known AML driver genes.

Supplementary Table 5. Public datasets used in this study
Summary of publicly available datasets used for analyses, including publication identifiers (PMIDs) and accession numbers for raw sequencing data.

Supplementary Table 6. List of super-enhancers
Super-enhancer regions identified from H3K27ac ChIP–seq data. Genomic coordinates, annotations, and their presence across ATAC-defined subgroups are provided.

Supplementary Table 7. Summary statistics of scRNA/ATAC-seq data
Quality metrics and summary statistics for single-cell datasets, including sample identity, number of cells, and sequencing-derived features such as detected genes per cell.

Supplementary Table 8. Differentially expressed genes in each ATAC subgroup
Top 3,000 differentially expressed genes for each ATAC subgroup ranked by statistical significance.

Supplementary Table 9. Differentially accessible chromatin regions in each ATAC subgroup
Top 3,000 differentially accessible chromatin regions (ATAC peaks) for each ATAC subgroup, ranked

by statistical significance.

Supplementary Table 10. Gene sets used for GSEA and GO analysis
Gene sets used for GSEA and Gene Ontology analysis.

Supplementary Table 11. Genes used for RNA-based prediction models (ClaNC)
Gene lists used for RNA-based subgroup prediction models using the ClaNC algorithm. These include gene sets for distinguishing all ATAC subgroups and for identifying high-risk subgroups within each ELN risk category.